Sensitivity of a Cloud-Resolving Model to Bulk and Explicit Bin Microphysical Schemes. Part I: Comparisons

XIAOWEN LI

Goddard Earth Science and Technology Center, University of Maryland, Baltimore County, Baltimore, Maryland

WEI-KUO TAO

Laboratory for Atmospheres, NASA Goddard Space Flight Center, Greenbelt, Maryland

ALEXANDER P. KHAIN

The Hebrew University of Jerusalem, Jerusalem, Israel

JOANNE SIMPSON

Laboratory for Atmospheres, NASA Goddard Space Flight Center, Greenbelt, Maryland

DANIEL E. JOHNSON

Goddard Earth Science and Technology Center, University of Maryland, Baltimore County, Baltimore, Maryland

(Manuscript received 12 October 2007, in final form 17 April 2008)

ABSTRACT

A two-dimensional cloud-resolving model is used to study the sensitivities of two microphysical schemes, a bulk scheme and an explicit spectral bin scheme, in simulating a midlatitude summertime squall line [Preliminary Regional Experiment for Storm-Scale Operational and Research Meteorology (PRE-STORM), 10–11 June 1985]. In this first part of a two-part paper, the developing and mature stages of simulated storms are compared in detail. Some variables observed during the field campaign are also presented for validation. It is found that both schemes agree well with each other, and also with published observations and retrievals, in terms of storm structures and evolution, average storm flow patterns, pressure and temperature perturbations, and total heating profiles. The bin scheme is able to produce a much more extensive and homogeneous stratiform region, which compares better with observations.

However, instantaneous fields and high temporal resolution analyses show distinct characteristics in the two simulations. During the mature stage, the bulk simulation produces a multicell storm with convective cells embedded in its stratiform region. Its leading convection also shows a distinct life cycle (strong evolution). In contrast, the bin simulation produces a unicell storm with little temporal variation in its leading cell regeneration (weak evolution). More detailed, high-resolution observations are needed to validate and, perhaps, generalize these model results. Interactions between the cloud microphysics and storm dynamics that produce the sensitivities described here are discussed in detail in Part II of this paper.

1. Introduction

Cloud-resolving models (CRMs) have made significant contributions toward the understanding of cloud and precipitation systems over the past four decades. With rapid advancement in computer power, more realistic physical processes (e.g., surface–air exchange, radiation, turbulent mixing, and topography) and better numerical methods (e.g., grid nesting, positive-definite advection scheme for scalar variables) have been incorporated into CRMs. These improvements, together with finer resolution, longer integration time, larger model domain, and more realistic initialization and large-scale forcing, have enabled progressively better simulations of cloud/precipitation processes in CRMs.

Corresponding author address: Xiaowen Li, Code 613.1, NASA GSFC, Greenbelt, MD 20770.
E-mail: xiaowen.li-1@nasa.gov

DOI: 10.1175/2008JAS2646.1

© 2009 American Meteorological Society

The microphysical schemes in CRMs have also been improved greatly over time. However, the majority of current CRMs still use "bulk" microphysical parameterizations, which is essentially a Kessler (1969)-type scheme. A bulk scheme specifies the particle size distributions of various hydrometeor types and typically solves prognostic equations of a mixing ratio for each type. The bulk scheme is conceptually simple and computationally efficient. However, bulk schemes cannot explicitly address questions related to variations in hydrometeor particle size or number concentration (e.g., aerosol–cloud–precipitation interactions and their impact on the global energy balance and climate change). "Two-moment" bulk schemes have been developed (e.g., Cotton et al. 1986; Murakami 1990; Wang and Chang 1993; Ferrier 1994; Meyers et al. 1997; Carrió and Nicolini 2002; Seifert and Beheng 2006; Morrison and Grabowski 2007) to partially address this problem by including representations of the mean particle sizes in CRMs. In addition to the mixing ratio, a two-moment bulk scheme also predicts particle number concentrations. This type of scheme still has to make crucial assumptions such as the activation of cloud condensation nuclei (CCN), the shapes of particle size distributions, and the mean terminal fall velocities of various particles.

"Bin" or "spectral bin" microphysical schemes have been widely used in basic microphysical studies. They were also the natural choice in many early cloud models, whose dynamics were relatively simple and whose simulations did not involve ice phase microphysics (e.g., Clark 1973; Soong 1974; Takahashi 1975). A bin scheme uses dozens, even hundreds, of particle size bins to represent the actual size spectra of CCN as well as different hydrometeor particles. Cloud droplet activation is explicitly calculated in a bin model, making it an indispensable tool in the study of aerosol indirect effects. Several bin schemes with both water and ice phase microphysics have been incorporated into cloud models (e.g., Hall 1980; Reisin et al. 1996; Khain and Sednev 1996; Ovtchinnikov and Kogan 2000). Cloud models with bin microphysical schemes have been used to study CCN–cloud interactions (e.g., Hall 1980; Khain et al. 1999, 2004, 2005; Tao et al. 2007), weather modification (e.g., Yin et al. 2000a), the effect of giant CCN (e.g., Yin et al. 2000b), and ice production mechanisms (e.g., Ovtchinnikov et al. 2000; Fridlind et al. 2004).

Although the main goal of developing a CRM with bin microphysics is to study aerosol–cloud–precipitation interactions, which cannot be achieved by using a simple bulk microphysical scheme, it is nevertheless a meaningful study to compare simulations between the two schemes. Despite the fact that the bin microphysical scheme is considerably more sophisticated than the bulk scheme (a 20-fold increase of computing time for this case study), the formulations of both schemes are based on the same theory and are self-contained. Both of them inevitably involve various assumptions at different scales. A detailed comparison of the bulk and bin microphysical scheme using the same model framework could reveal the strengths and weaknesses of both schemes. It may also help to answer such important questions as how various microphysical processes interact with cloud dynamics, shape the precipitation system structure, and affect their environment. In additional, this study also serves to validate the newly incorporated bin scheme using relatively well established bulk scheme simulations. In the early stages of CRM development, Soong (1974) and Shiino (1983) used axisymmetric models to study the sensitivity of their models to bulk and bin microphysical schemes for a warm, maritime, small cumulus cloud. They both found that the bulk scheme simulation produced an earlier onset of surface rainfall compared with the bin scheme simulation. Different cloud structures were also simulated using different schemes. However, these earlier cloud models had a limited dynamical framework and simplified microphysics (e.g., warm rain only) and simulated only a single, shallow cloud. It is to be expected that shallow, short-lived clouds are sensitive to changes in the formulation of microphysical processes because of the relatively weak dynamical forcing in this cloud type. For deep convection, such as a long-lasting mesoscale convective system (MCS) studied in this paper, strong dynamics could dominate the relatively small variations caused by the different microphysical schemes.

This paper presents a detailed comparison between simulations using the bulk and bin microphysical schemes with both warm rain and ice microphysics for a midlatitude, summertime squall line case. In contrast to the earlier sensitivity studies described above, which focused mainly on the developing stage of a single cumulus cloud, this study focuses on the quasi-steady state achieved in the simulated squall system. The quasi-steady state achieved in the model is insensitive to various artificial initial perturbations (e.g., cool pool, hot bubble), adding more confidence in this comparison study. Published observations of the same case, mainly derived from multiple Doppler radar analysis and sounding data, are included wherever applicable to validate the model. A direct validation of the bin microphysical scheme requires detailed microphysical observations, especially in situ measurements, which we hope to be able to carry out in the future.

In the next section, a brief description of both the

CRM and bin microphysical scheme are given, together with a general description and model setup for the 10–11 June 1985 Preliminary Regional Experiment for Storm-Scale Operational and Research Meteorology (PRE-STORM) case. In section 3, simulations by the bulk and bin schemes are compared with each other and with some available observations in terms of general rainfall features, kinematic and thermodynamic characteristics, and the heat budget. The emphasis in this section is on the differences between the simulations using different schemes during their quasi-steady states. Diagnostic analyses and sensitivity tests aimed at identifying the microphysical processes responsible for these differences will be presented in Part II of this paper (Li et al. 2009, hereafter Part II). The PRE-STORM case is perhaps one of the best-studied continental MCSs. The plots in section 3 are constructed in order to take advantage of the many previously published observations of this case. A summary is given in section 4.

2. Model and case descriptions

a. Cloud-resolving model

The CRM used in this study is the 2D anelastic version of the Goddard Cumulus Ensemble (GCE) model with open lateral boundaries and a free slip upper boundary with absorption layers near the top. The 2D framework is suitable because the PRE-STORM case is a typical MCS system with relatively small variations along the line (Houze 1993; Biggerstaff and Houze 1993). Furthermore, previous CRM simulations (e.g., Weisman et al. 1988; Fovell and Dailey 1995; Parker and Johnson 2004) demonstrated that the dynamical structures in 2D and 3D simulations of a MCS system are similar. The current model includes both solar and infrared radiation and a bulk aerodynamic surface flux scheme (Tao et al. 1996). The subgrid-scale turbulence in the GCE model is based on Klemp and Wilhelmson (1978). The bulk microphysical scheme is based on Lin et al. (1983) with prognostic equations for mixing ratios of cloud water, rain, ice, snow, and hail. Condensation/evaporation of cloud droplets uses instantaneous adjustment, that is, water vapor above supersaturation is converted to cloud water within one time step, and cloud water evaporates until depleted or the environment reaches saturation. Rain evaporation is calculated by integrating evaporation of individual raindrops over a Marshall–Palmer size distribution (Lin et al. 1983). All scalar variables use a forward-in-time, positive-definite advection scheme with a nonoscillatory option (Smolarkiewicz and Grabowski 1990). Details on the GCE model can be found in Tao and Simpson (1993) and Tao et al. (2003a).

b. Bin microphysical scheme

The bin microphysical scheme in the Hebrew University Cloud Model (HUCM) explicitly describes the size spectra of seven hydrometeor types: cloud/rain, three types of ice crystals (plate, column, and dendrite), snow/aggregates, graupel, and hail/frozen drops, as well as CCN. The size spectrum of each hydrometeor type is represented by 33 mass doubling size bins (i.e., the mass of the kth bin $m_k = 2m_{k-1}$, where $m_1 = 3.4 \times 10^{-11}$ g corresponds to the smallest water droplet radius of $r_1 \approx 2\ \mu$m). The bin scheme solves equations of the discrete particle number concentration $f_{i,k}$ ($f_{i,k}dm_k$ is the particle number per unit volume of air whose masses are between m_k and $m_k + dm_k$), where $i = 1, 7$ represents the types of different hydrometeors and $k = 1, 33$ represents the particle sizes. Advection of the term $f_{i,k}dm_k$ uses the same scalar advection scheme in the GCE model. The microphysical terms can be illustrated as

$$\left(\frac{\partial f_{i,k}}{\partial t}\right)_{\text{micro}} = \text{nucleation} + \text{diffusion} + \text{coagulation} + \text{breakup} + \text{multiplication} + \text{freezing} + \text{melting}. \quad (1)$$

The nucleation term applies to cloud droplets and ice crystals. Cloud droplets are activated explicitly according to the size distribution of CCN, which is also represented by 33 mass size bins with the maximum size bin the same as the smallest cloud droplet size bin. The sizes of newly activated cloud droplets are calculated according to the Kölher equation (Pruppacher and Klett 1997) except when the dry CCN radius is larger than 0.03 μm. Since large CCN take a long time to achieve their equilibrium, the cloud droplet radius formed from large CCN is assumed to be five times its dry CCN radius (e.g., Kogan 1991). Concentrations of the deposition and condensation-freezing ice nuclei are based on Meyers et al. (1992). Ice crystals with different shapes (column, plate, or dendrite) form at different temperature and relative humidity regimes. Diffusional growth (condensation/evaporation, deposition/sublimation) requires information of the supersaturation with respect to water (S_w) and ice (S_i). In the bin scheme, S_w and S_i are solved analytically for the condition with coexisting vapor, water, and ice. They are then used to solve for individual particle growth. The integrations of the individual particle growths determine the change of the vapor field and the correspond-

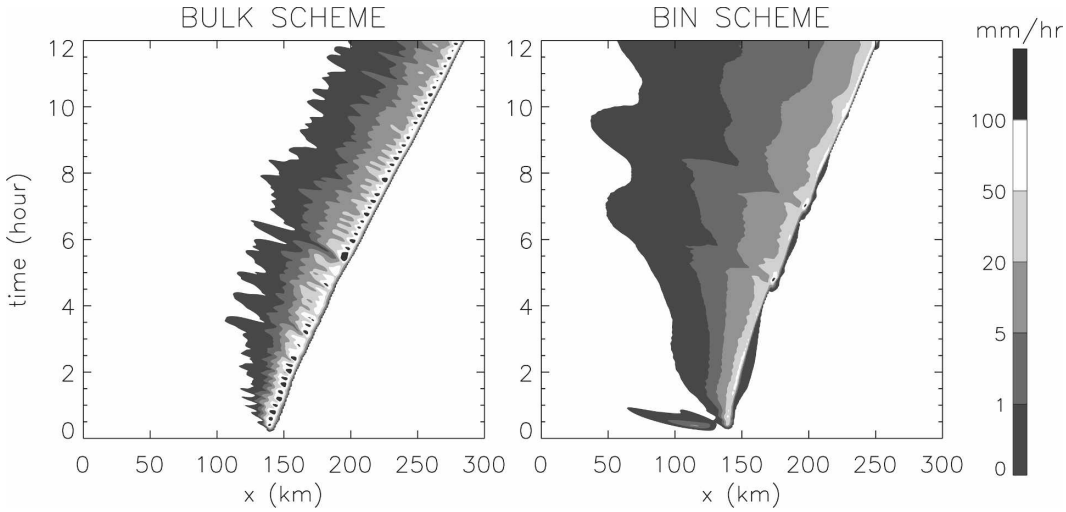

FIG. 1. The time-domain diagram of surface rainfall for the (left) bulk and (right) bin scheme simulations.

ing latent heat exchanges (Khain and Sednev 1996; Reisin et al. 1996). Stochastic kinetic equations for drop–drop, drop–ice, and ice–ice collision/coalescence and for collisional breakup of raindrops are solved using Bott's (1998) scheme. These stochastic equations represent the coagulation and breakup terms in Eq. (1). Ice multiplication is formulated according to Hallett and Mossop (1974) and occurs between −3° and −8°C. The heterogeneous freezing of drops uses the immersion ice nuclei formula from Vali (1975) and the contact ice nuclei formula from Meyers et al. (1992). Homogeneous freezing becomes important below about −35°C. The melting of ice particles is calculated explicitly by solving prognostic equations for water fractions in each ice particle bin (Phillips et al. 2007). Details of the bin scheme can be found in Khain and Sednev (1996) and Khain et al. (2000, 2004).

c. *Experiment design*

The 10–11 June 1985 PRE-STORM case is a well-documented midlatitude MCS (e.g., Johnson and Hamilton 1988; Rutledge et al. 1988). The GCE model is initialized with a single sounding taken ahead of the forming squall line. There are 33 stretched vertical levels with a resolution of 240 m at the lowest level and 1250 m at the top. The horizontal grid number is 1024 with 1-km resolution for the center 872 points; outer grids are stretched at the lateral boundaries. The total integration time is 12 hours with $\Delta t = 6$ s. A low-level cool pool is applied for the first 10 min to initialize the convection. A modified horizontal wind profile with low-level shear of about 20 m s^{-1} over the depth of 3.5 km is also applied. Further details of the experiment design and initial conditions for the bulk scheme simulation can be found in Tao et al. (1993).

The bin simulation uses exactly the same model setting as the bulk run. The only difference is the microphysics. Additional initial aerosol information is needed for the bin scheme simulation. Owing to the lack of CCN observations for this case, an idealized CCN spectrum is used according to Twomey and Wojciechowski (1969):

$$N_{\mathrm{CCN}} = CS^k, \tag{2}$$

where N_{CCN} is the CCN number concentration (cm^{-3}) and S is the supersaturation with respect to water; C and k are constants that may change with location, time, height, and air parcel history. In this study, C = 600 cm^{-3} and k = 0.308 are used in an attempt to represent a typical background CCN spectrum over the continent (Pruppacher and Klett 1997). No giant CCN are included.

Sensitivity tests using 500-m horizontal resolution have been carried out for both bulk and bin schemes. The mean storm structure remains the same in both cases. The vertical resolution used in this study is rather coarse for explicitly simulating CCN activations. However, separate sensitivity tests show that wide ranges of variations in activated cloud droplet number concentrations do not affect the overall storm structure (Tao et al. 2007).

3. Comparisons

The simulated MCS evolution can be illustrated by the surface rainfall time–domain plots in Fig. 1. Rain

from a single, initial deep convective cell reaches the ground within 20 min in both cases, with the bin simulation slightly later than in the bulk scheme. During the developing stage (the first 6 h), new convection is generated at the leading edge of the squall. The precipitation systems propagate forward (rightward) relative to the modeling frame, which also moves rightward relative to the ground at a constant speed of about 12 m s^{-1}. The trailing stratiform rain area expands gradually until it reaches its maximum after about 6 h. Both MCSs then settle into quasi-steady states with a leading convective edge and a trailing stratiform region. The development of the simulated systems agrees qualitatively with the surface radar observations of Rutledge et al. (1988), which shows the surface precipitation area expanding from about 110 km with a limited stratiform rain area to more than 180 km with an extensive stratiform rain area within about 2 h (Figs. 4 and 5 in Rutledge et al. 1988). The dissipation stage of the MCS cannot be simulated by the current model setup. After reaching the mature stage, the simulated system becomes quasi-steady. The emphasis of this paper is to compare the quasi-steady states simulated by the different microphysical schemes.

a. Surface rainfall and radar reflectivity

1) SURFACE RAINFALL

The most significant difference in terms of surface rainfall simulation is that the bin scheme has a much larger trailing stratiform area than the bulk scheme. Lynn et al. (2005) found similar results using the bin microphysical scheme in a regional model. At t = 12 h the width of the rain area is about 180 km in the bin simulation compared with about 80 km in the bulk simulation, as shown in Fig. 1. Consequently, light rain contributes significantly more to the total surface rainfall in the bin simulation. Figure 2 shows the probability density function using instantaneous surface rain rates at 1-min intervals. For the bin scheme, roughly a quarter of the accumulated surface rainfall over the 12-h period comes from light rain with intensities less than 10 mm h^{-1}, whereas the same light rain category contributes to only 8% of the total rainfall in the bulk simulation. In the meantime, less than 1% of the total surface rainfall comes from heavy rain of more than 100 mm h^{-1} in the bin simulation compared with about 9% in the bulk simulation. Johnson and Hamilton (1988) used densely deployed rain gauge data collected during the passage of the 10–11 June PRE-STORM squall line to quantify the contribution of the stratiform rain. In their study, convective rain is assigned when the rainfall rate is above 6 mm h^{-1}. They found that an average of

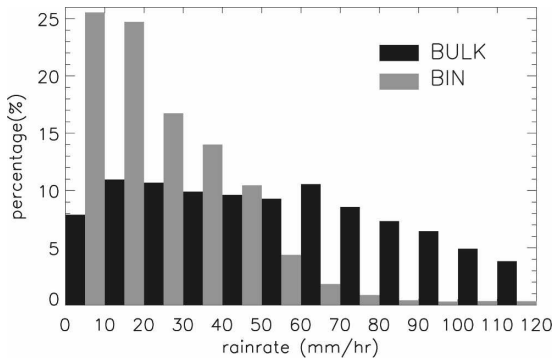

FIG. 2. Simulated surface rainfall probability density function for the bulk scheme (black bars) and the bin scheme (gray bars). The x axis is the instantaneous surface rainfall bins at 10 mm h^{-1} intervals; the y axis is the percentage contribution of each bin toward the total surface rain accumulation.

29% of the surface rain comes from the stratiform region. When the same criteria are applied to the model-simulated surface rainfall during the mature stage (the last 6 h of the simulation), about 20% of the total surface rainfall is stratiform in the bin simulation compared with only 7% in the bulk simulation. While both simulations underestimate the amount of light rain compared to observations, the bin scheme produces significantly more stratiform rain over an extensive area.

Another significant difference between the two plots in Fig. 1 is the high rainfall rate streaks simulated by the bulk scheme, which extend from the leading convection well into the stratiform region, and the lack thereof in the bin simulation. These high surface rainfall streaks are the manifestations of rearward propagating convective cells, identifiable well into the trailing stratiform region, as shown in Fig. 3.

2) RADAR REFLECTIVITY

Figure 3 compares the observed radar reflectivity at 0345 UTC 11 June 1985, during the mature stage of the PRE-STORM squall (Rutledge et al. 1988), to the simulated instantaneous radar reflectivity at t = 12 h. The spatial scales and contour levels are matched in all three panels. Radar reflectivity in the bulk model is calculated using fixed, exponential particle size distributions and densities, whereas simulated particle size distributions are used in the bin model.

Large differences exist between the instantaneous radar reflectivity structure simulated by the bulk and bin schemes, especially in the stratiform region. Both the size and fraction of the stratiform rain are much larger in the bin simulation, which is also evident in Figs. 1 and 2. The stratiform region in the bin simulation (Fig. 3b)

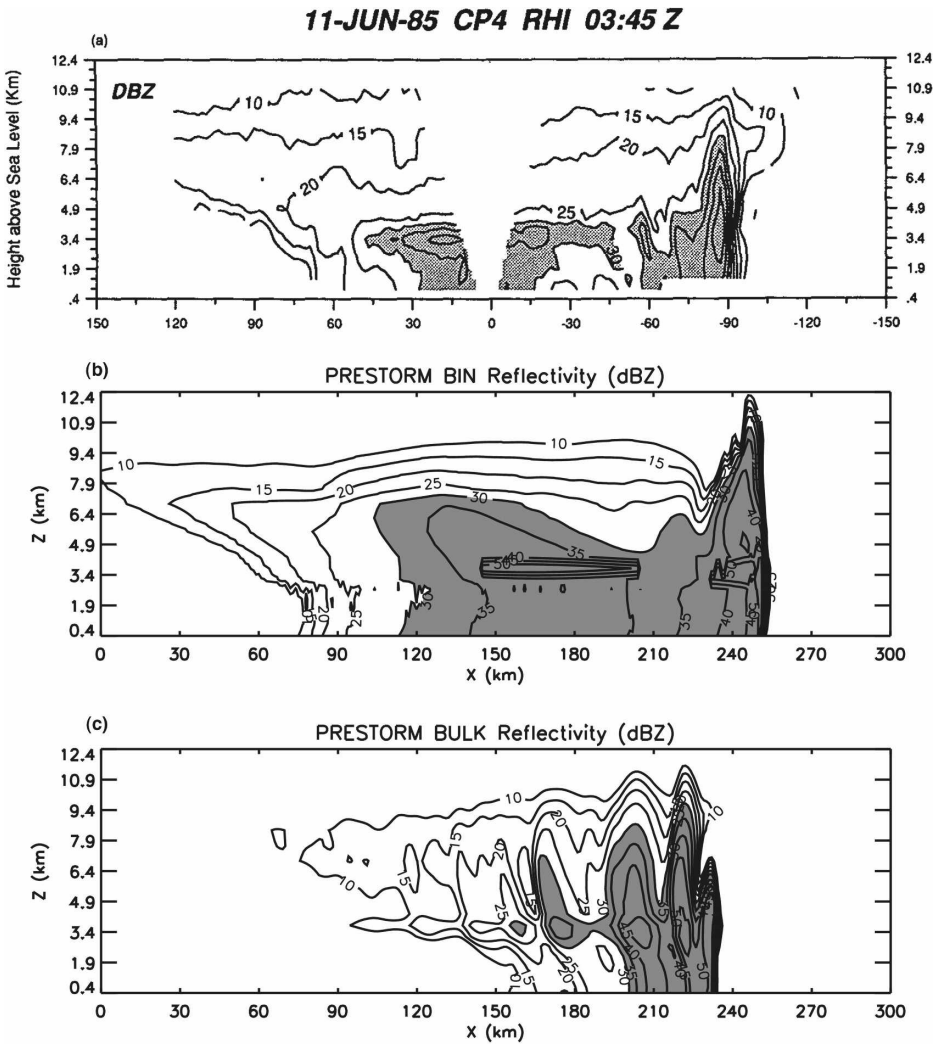

FIG. 3. Comparison of the (a) observed radar reflectivity with the simulated instantaneous radar reflectivity for the (b) bin and (c) bulk schemes. Observed radar reflectivity during the mature stage of the storm is copied from Fig. 5 in Rutledge et al. (1988). The simulated radar reflectivity is the instantaneous value at $t = 12$ h, well into the quasi-steady state. Areas with radar reflectivity larger than 30 dBZ are shaded and contours are at 5-dBZ intervals.

is homogeneous, with no sign of convective cells embedded. On the other hand, cellular convective structures in the form of high radar reflectivity cores are evident even to the rear end of the stratiform region in Fig. 3c. These cells are remnants of the previous leading convections that propagate rearward while decaying progressively. At this particular time, a total of five cells are visible in Fig. 3c, located at $x \sim 233$ km, 226 km, 210 km, 180 km, and 160 km.

Radar reflectivity observations of the PRE-STORM squall have been studied in many papers (e.g., Smull and Houze 1987a,b; Rutledge et al. 1988; Rutledge and MacGorman 1988; Biggerstaff and Houze 1993). The widespread trailing stratiform region observed in these studies compares better with the bin simulation, as shown in Fig. 3. Convective cells embedded within the stratiform region were not reported in these observational studies (e.g., Fig. 3). However, Rutledge and Petersen (1994) have found evidence of cloud water coexisting with ice in the stratiform region for this PRE-STORM case, which may be produced by weak convective cells. Additional high-resolution radar observations are needed to determine how often the convective cells exist in the stratiform region in a MCS and to further validate the stratiform rain structure simulated by different microphysical schemes.

Differences in radar reflectivity patterns also exist in the leading convective zone for the two simulations. In

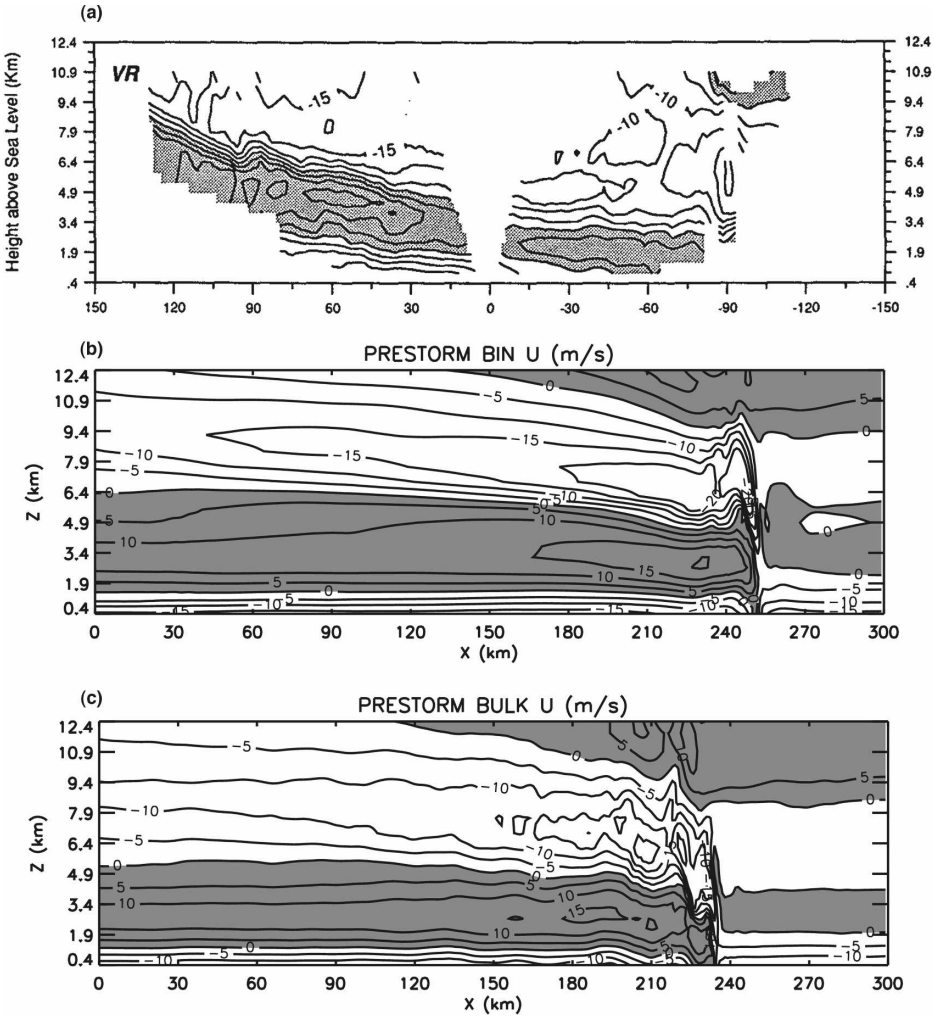

FIG. 4. As in Fig. 3 but for the instantaneous horizontal wind fields. The shaded area represents winds coming from the left; contours are every 5 m s^{-1}.

the bulk simulation, the radar echo top of the leading cell is generally below 7 km, and the second cell is always the tallest with its top above 10 km throughout the quasi-steady state stage. On the other hand, the leading cell is almost always the tallest in the bin simulation. A weak transition zone, which is a local radar reflectivity minimum between the convective and stratiform region, is located at $x \sim 210$ km in Fig. 3b. The transition zone is a common feature observed in MCSs (e.g., at $x \sim -50$ km in Fig. 3a). The multicell system simulated by the bulk scheme does not have a well-defined transition zone. Another common signature in the widespread stratiform region of an MCS is the bright band, a local maximum in radar reflectivity near the 0°C level produced by the melting of large ice particles. Both bulk and bin simulations show brightband signatures at a height just below 4 km, which agrees qualitatively with observations. In the model simulations, it is assumed that the radar reflectivity of a melting particle is the same as that of a water drop of the same size (i.e., an ice particle with water coating). This results in an overestimation of the brightband reflectivity, as evident in Figs. 3b and 3c.

b. *Kinematics and dynamics*

1) HORIZONTAL WIND

The horizontal wind field in a mature MCS exhibits rather robust structures as summarized in Houze (1993). Figure 4 shows the observed and simulated instantaneous horizontal wind fields at the same time as for Fig. 3. Identical spatial scales and contours are used in all panels. Similar to the observation in Fig. 4a, a deep front to rear (FTR) outflow exists at mid to upper

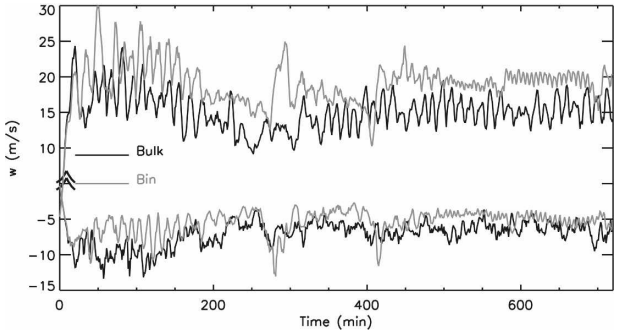

FIG. 5. Time series of the maximum and minimum vertical air velocity (m s^{-1}) for the bulk (gray lines) and bin (black lines) scheme: data points are every 1 min for 720 min.

levels, partly fed by the leading convection. This FTR outflow is responsible for carrying the ice particles generated in the leading convection rearward into the stratiform region. Dominating the lower to middle levels is a rear to front (RTF) inflow (shaded in Fig. 4), which is maintained by diabatic heating. Its descent to the leading edge is forced by evaporative cooling and water loading. (Smull and Houze 1987b; Zhang and Gao 1989; Szeto and Cho 1994; Pandya and Durran 1996). A near-surface, FTR flow prevails below about 1.5 km.

Several discrepancies exist between both simulations and the observation in Fig. 4. The most prominent one is the origin of the RTF inflow. The RTF inflow originates above 9 km in the observation, but below 6 km in both simulations. The lack of interaction with the environment and the limitation of the 2D framework of the current CRM may explain this. Zhang and Gao (1989) successfully reproduced the observed rear inflow structure for the same 10–11 June PRE-STORM case using a nested grid mesoscale model. Sensitivity tests from their study revealed that, when the large-scale evaporative cooling was turned off, the RTF inflow still originated at about 9 km but it became weaker and did not penetrate to the ground. They argued that large-scale baroclinity, which is not included in our 2D framework, was responsible for the high origin and, partly, the strength of the RTF inflow. In addition, large-scale baroclinity may also contribute to the second jet core located at $x \sim 60$ km in Fig. 4a, which is missing in both Figs. 4b and 4c.

2) VERTICAL WIND

Time series of the maximum vertical velocity is a good indicator of cell regeneration cycles in a 2D framework (e.g., Fovell and Dailey 1995). In Fig. 5, the maximum and minimum vertical velocities simulated by the different schemes are plotted for the 12-h period. It is readily apparent that there are certain periodicities in the temporal variations in Fig. 5, similar to some examples discussed in Fovell and Dailey (1995). Wavelet analyses (e.g., Torrence and Compo 1998) of the maximum vertical velocity time series reveal that for the first 200 min (i.e., during the system's developing stage) the dominant oscillation period is 12∼16 min for both bulk and bin simulations. Some kind of transitional stage occurs between 200 and 300 min for the bulk model (200–400 min for the bin model), which has irregular oscillations. After about 400 min, during the mature stage of the system, the dominant oscillation period in the bulk simulation settles back to a value of 12∼16 min, whereas the bin simulation is characterized by 5∼6-min oscillations with much weaker amplitudes than the bulk simulation.

As shown in Fig. 5, cell regeneration cycles have different periods during the mature stage of the two simulations. To illustrate the different quasi-steady states achieved by the different microphysical schemes, the vertical velocity field sequences are plotted in Figs. 6 and 7. Vertical air velocities are contoured at 1 m s^{-1} intervals, with the negative values dashed. Figures 6a–f roughly capture the life cycle of a regenerating leading convective cell during the mature stage of the bulk simulation. In Fig. 6, multiple convective cores can be identified as cellular structures with w larger than 1 m s^{-1}. Similar "multicell" structures in the w field have been reported in many previous model studies, both in 2D and 3D frameworks (e.g., Fovell and Ogura 1989; Lin and Joyce 2001). In Fig. 6, as the leading cell grows, it leans progressively rearward (Figs. 6a–c). The near-surface convergence in front of the leading cell, generated by the cold outflow and the ambient lower-level inflow, forms the embryo of a new cell at $x \sim 90$ km in Fig. 6c. The rapid growth of this new leading cell can be clearly seen from Figs. 6c and 6d, where the previous leading cell (located at $x \sim 77$ km in Fig. 6d) moves rearward and starts to lose its intensity. In Fig. 6f, the new leading cell becomes independent and is separated from the previous leading cell by a deep downdraft core formed by the merger of the lower-level downdraft core, driven mainly by evaporative cooling and precipitation loading, and the upper level downdraft core, driven mainly by compensating downdrafts (Fig. 6e). The previous leading cell ($x \sim 75$ km in Fig. 6f), now totally cut off from the feeding of the near surface FTR inflow, weakens considerably but is still active. Back in Fig. 6a, the previous leading cell is located at $x \sim 72$ km. It splits from a previously merged cell, briefly shrinks, and intensifies (Figs. 6b and 6c) before dissipating into a small updraft core in Fig. 6f at $x \sim 57$ km. Some of the rearward propagating cells merge with a lower-level updraft core and become a deep convective core (e.g., $x \sim$

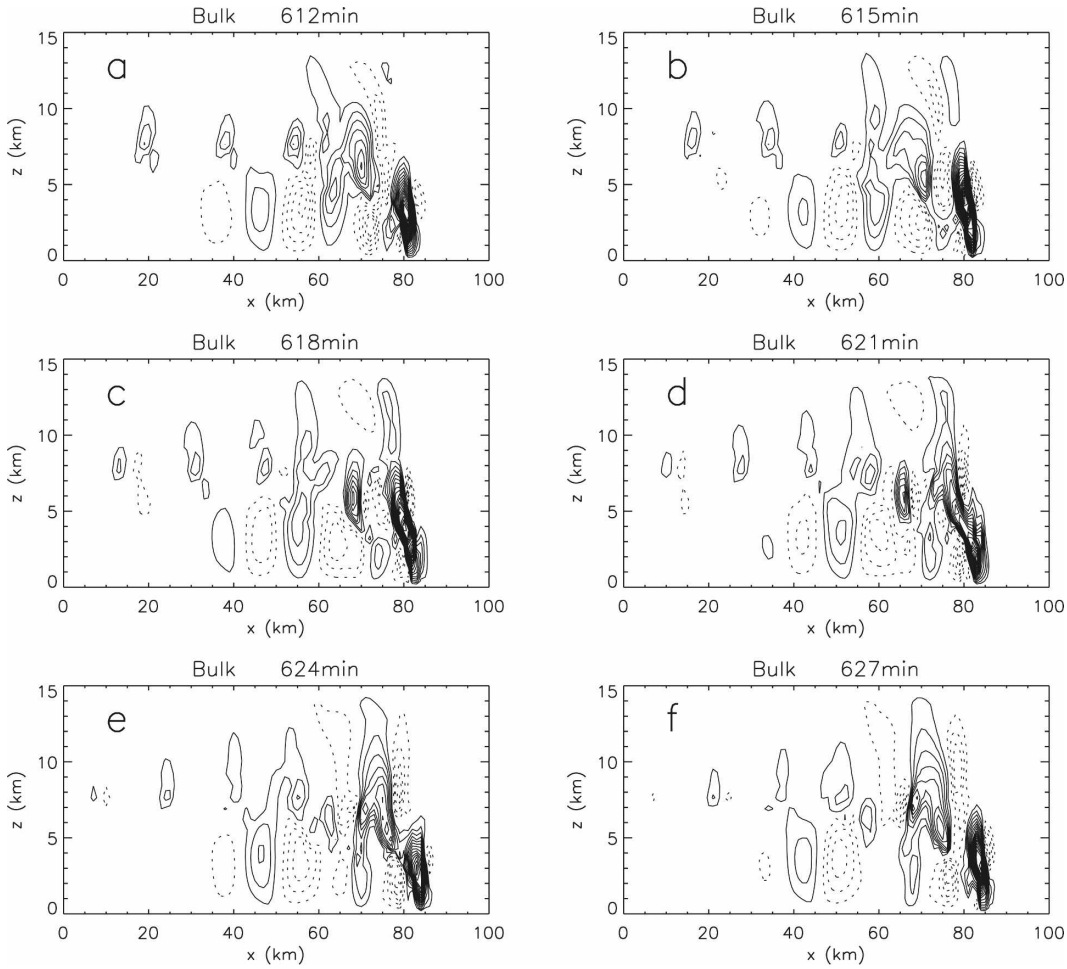

FIG. 6. Bulk scheme simulated instantaneous vertical air velocity fields every 3 min starting at $t = 612$ min, roughly representing the life cycle of a regenerating new cell at the leading edge of the squall line. Contour interval is 1 m s^{-1} with positive velocities in solid lines and negative velocities in dashed lines.

55 km in Fig. 6c). This type of cell merger results in a relatively strong convective cell structure within the stratiform region. Although cell regeneration is not strictly repetitive, as evidenced in the vertical velocity time series in Fig. 5, the characteristics described in Fig. 6 are consistent throughout the bulk simulation. Furthermore, the cell regeneration cycle described in Fig. 6 is consistent with many previous studies of multicell storms (e.g., Fovell and Tan 1998; Lin and Joyce 2001; Yang and Houze 1995).

Figure 7 is the same as Fig. 6 except for the bin scheme simulation. The time evolution of the leading cell in Fig. 7 is quite different from Fig. 6. During the 15-min period shown in Fig. 7, only a single updraft core exists. This updraft core has its own weak oscillations with a period of about 6 min (Fig. 5). A much weaker second cell (i.e., $x \sim 33$ km in Fig. 7a) exists but is no longer active. The leading cell, termed a "unicell" here in contrast to the multicell structure in Fig. 6, has less of a rearward tilt compared with the bulk simulation, especially at lower levels. The leading updraft core maintains a quasi-steady structure and evolves rather continuously from $x \sim 54$ km in Fig. 7a to $x \sim 56$ km in Fig. 7f.

Two different cell structures and regeneration modes have been identified in the 2D simulations: the multicell structure, with a distinct leading cell regeneration cycle, is a consistent feature in the bulk simulation; the unicell structure with weak temporal variations dominates the quasi-steady state achieved in the bin simulation. However, a relatively weak multicell mode still exists during the first 2 h (the developing stage) of the bin simulation (plot omitted). Occasionally, bin simulation experiences distinct cell regeneration cycles too, shown as an example in Fig. 8. The difference between Figs. 6 and 8 is that the cell regeneration in Fig. 8 is

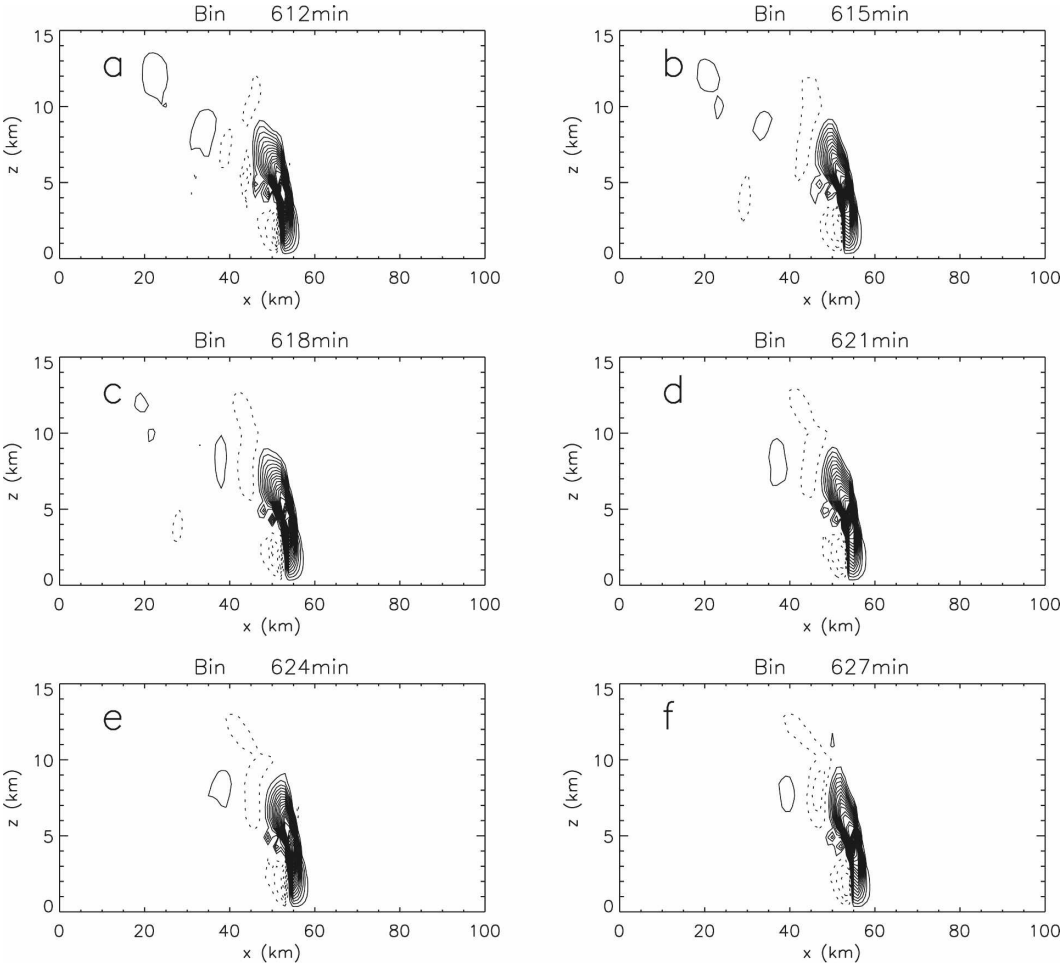

FIG. 7. As in Fig. 6 but for the bin microphysical scheme.

more discrete, similar to the discrete propagation described in Fovell et al. (2006). This type of discrete propagation happens only several times during the entire bin simulation, in contrast to the strong evolution described in Fig. 6, which is a consistent feature in the bulk simulation.

Observational evidence of the unicell structure is summarized in the schematic diagram in Fig. 9 (copied from Fig. 19 in Foote and Frank 1983), based on a triple-Doppler radar analysis. The first column in Fig. 9 illustrates the multicell structure, similar to the bulk simulation in Fig. 6. The multicell mode is termed "strong evolution" in Foote and Frank (1983) because of its distinct cell regeneration cycle. The middle column, which is termed "weak evolution", resembles the unicell structure in Fig. 7. In the weak evolution regime, the updraft core does not split but undergoes some internal oscillations. A similar weak evolution mode was also simulated by Fovell and Ogura (1989). The supercell model described in the last column refers to quasi-steady storms with a highly 3D structure (e.g., Weisman et al. 1988), which is not represented in the current 2D model framework.

As summarized by Fig. 9, both multicell and unicell structures have been observed previously. The question is: To which category does the 10–11 June PRE-STORM MCS belong? High-frequency vertical velocity observations are not available for this case. However, a time- and domain-averaged vertical air velocity field, retrieved from composite dual-Doppler radar data (Biggerstaff and Houze 1993), is available for comparison and provides some indication. The mean vertical motion field (Fig. 3d in Biggerstaff and Houze 1993) is reproduced in Fig. 10e. To compare with Fig. 10e, radar reflectivity averaged over the mature stage (5-min interval during the last 6 h of simulation) is plotted in Figs. 10a and 10b for the bulk and bin scheme. The corresponding average vertical air velocities are contoured in Figs. 10c and 10d. When averaged, the vertical cellular structures in the stratiform region simu-

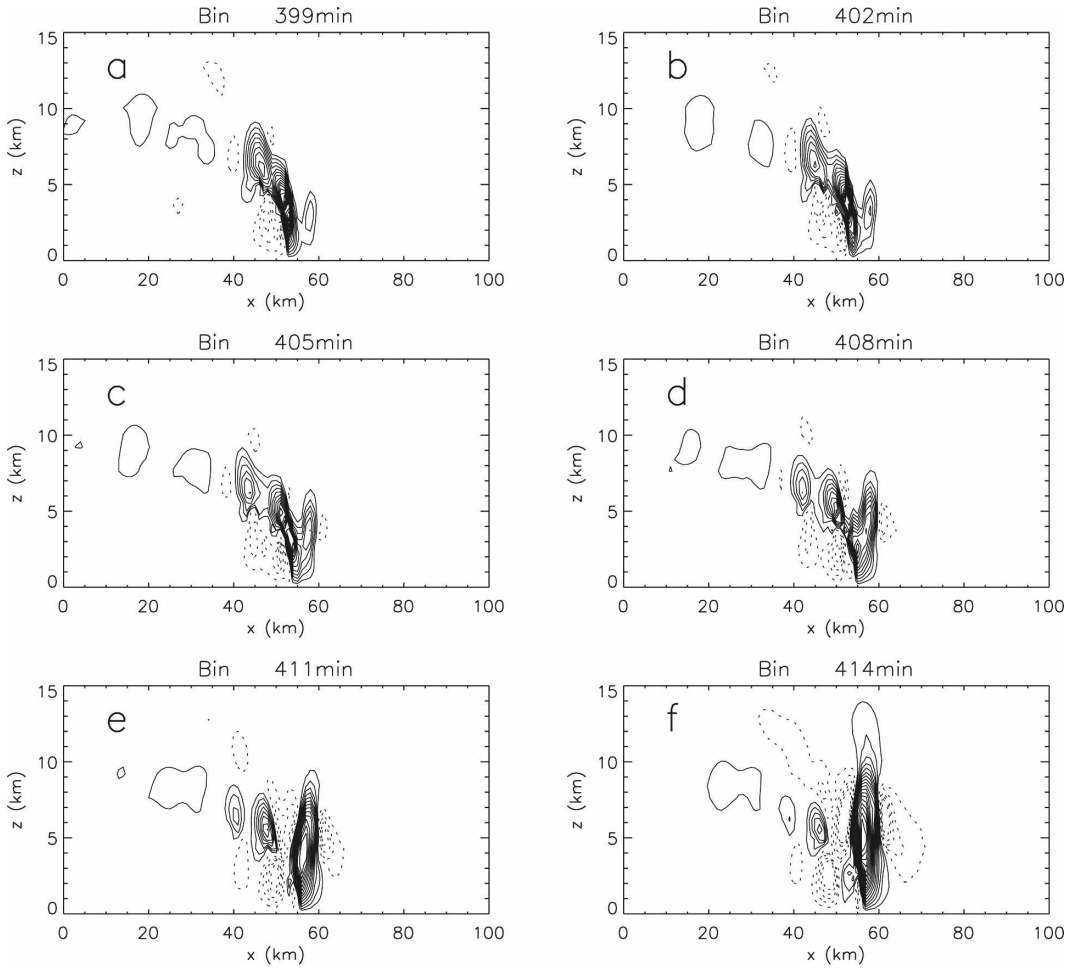

FIG. 8. As in Fig. 7 but for the time period of a discrete propagation with multiple cells and strong evolution in the bin simulation.

lated by the bulk scheme are smoothed out. Only the leading convection remains a robust cell structure. However, the size of the stratiform region simulated by the bulk scheme remains significantly smaller compared with the bin simulation in Fig. 10b.

The average mean vertical motion field for the bin simulation (Fig. 10d) remains very similar to its instantaneous fields (e.g., Fig. 7), providing additional evidence of the weak evolution mode simulated by the bin scheme. In Fig. 10d, a deep, leading updraft core is separated entirely from the much weaker and widespread updraft to the rear of the system by a deep downdraft core with two centers located at 2 and 8 km, respectively. These features can also be identified in the observations in Fig. 10e. For the bulk simulation, although the leading updraft core is sometimes completely separated from the second core by a deep downdraft (e.g., Figs. 6a and 6f), this feature does not appear in the time-averaged *w* field in Fig. 10c. Averaging the train of updraft cores traveling rearward results in a weak updraft area immediately behind the leading core with downdrafts both above and below it. If the strong evolution mode involves continuously rearward propagating updraft cores, as simulated in this and many previous studies (e.g., Fovell and Tan 1998; Lin and Joyce 2001; Yang and Houze 1995), it is unlikely that a consistent deep downdraft core will exist immediately behind the leading cell after time averaging. Furthermore, the leading updraft core in the bin simulation extends much higher, to about 15 km, than the shallow leading updraft core, which extends to only about 6 km in Fig. 10c. Thus, it appears that the observed vertical air velocity field compares better with the bin simulation and supports a mainly weak evolution mode during the mature stage of this PRE-STORM case. However, high-frequency vertical air velocity observations are needed for a definitive answer.

In the stratiform region, both Figs. 10c and 10d have

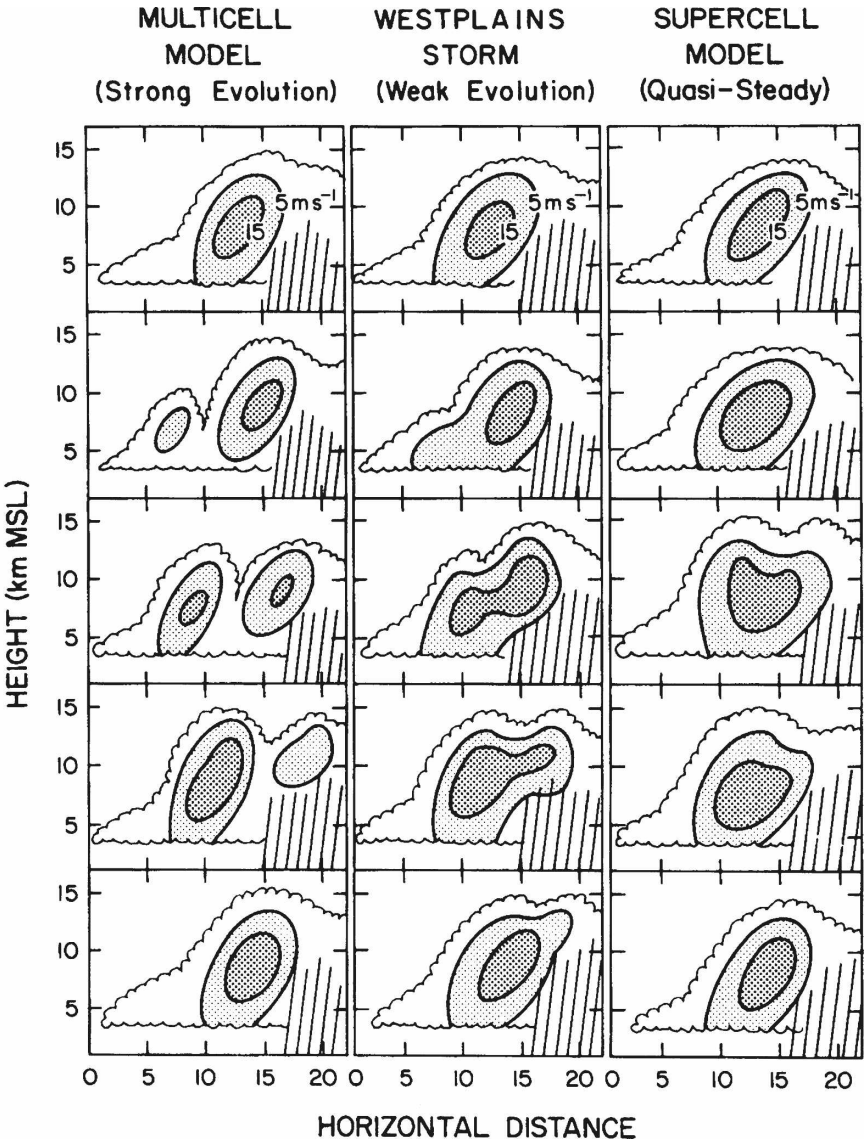

FIG. 9. Schematic diagram showing the updraft evolution for three different storm models: (left) the cellular evolution according to the multicell model, involving the formation of discrete updrafts; (right) the supercell model, with the updraft shown as being quasi-steady; (middle) the model deduced for the Westplains storm; here the large updraft undergoes gradual changes but remains singly connected. This is termed weak evolution, in contrast to the strong evolution of the multicell case. The time between successive frames, moving down the figure, is meant to be 3–5 min: contours represent isotachs of vertical wind speed. Figure and caption are copied from Fig. 19 in Foote and Frank (1983).

weak updrafts at upper levels and weak downdrafts at lower levels, which agree qualitatively with both the dual-Doppler analysis shown in Fig. 10e and the extended-velocity azimuth display (EVAD) analysis by Rutledge et al. (1988, their Figs. 8b, 13, and 14). There are some discrepancies between both simulations and the observations in Fig. 10. The most prominent ones are the size and magnitude of the leading convective core. Both simulations have a much stronger leading updraft core with maximum $w > 10$ m s^{-1}, compared with about 4 m s^{-1} in the observation. In the meantime, the simulated leading core sizes are 10~15 km compared with ~30 km in Fig. 10e. The wider and weaker leading core in the observation might be due to the method of time averaging. For example, an individual dual-Doppler analysis shown in Fig. 6 of Biggerstaff and Houze (1993) has a leading updraft core of about 10 km with maximum $w = 14$ m s^{-1}.

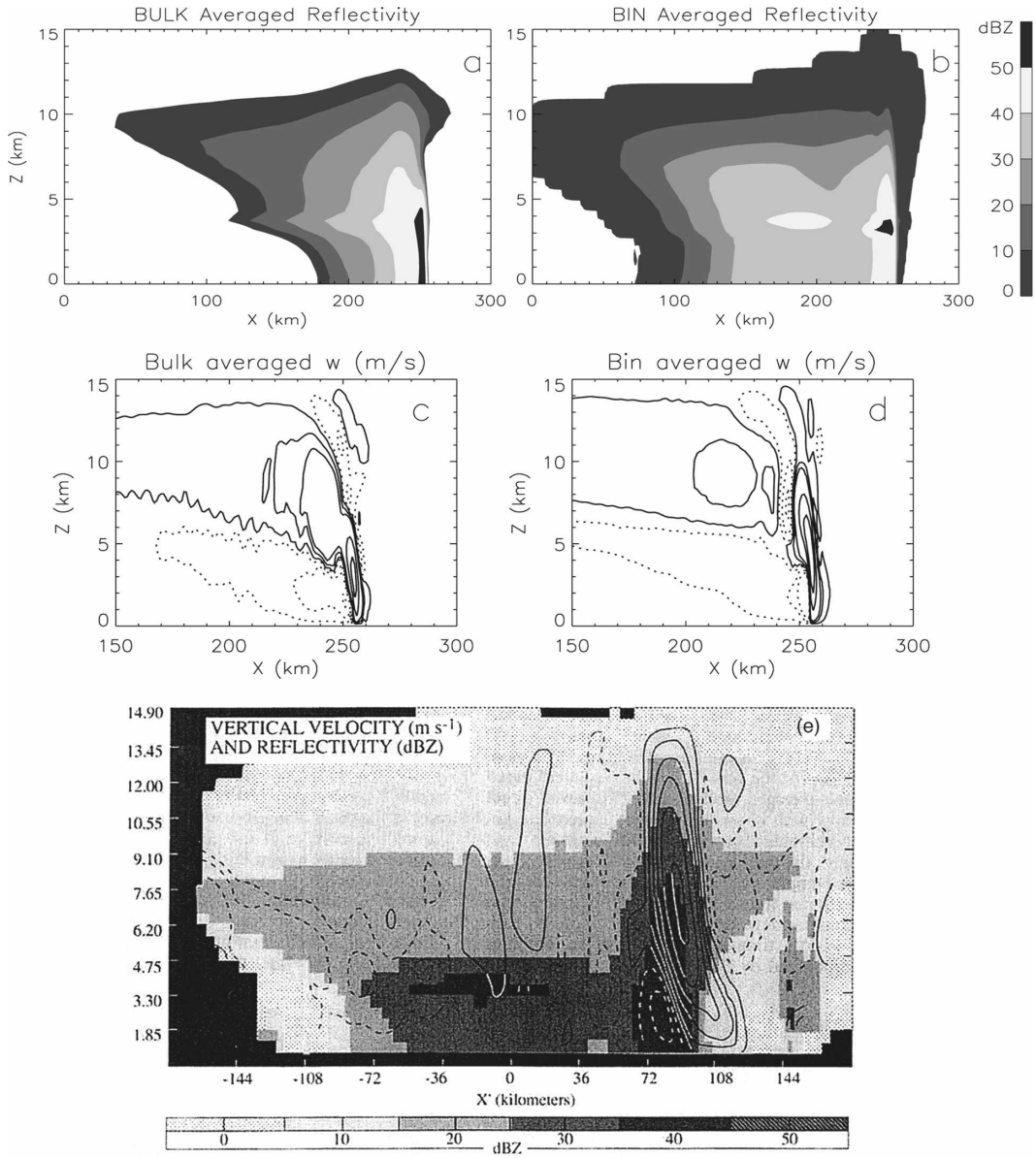

FIG. 10. Comparison of average radar reflectivity and vertical air velocity between the bulk and bin scheme simulations and observations. Simulations are averaged over the last 6 h, during the quasi-steady state of the storm. Average radar reflectivity for the (a) bulk and (b) bin simulation; average vertical air velocity for the (c) bulk and (d) bin simulation. Contours are at −1, −0.5, −0.1, 0.1, 0.5, 1, 5, 10, and 15 m s^{-1}. (e) Doppler radar composite analysis of along-line-averaged vertical cross section during 11 scans between 0131 and 0510 UTC 11 June 1985. The grayscale image is the radar reflectivity. Contours are the vertical air velocities at −0.9, −0.45, −0.15, 0.15, 0.45, 0.9, 1.5, 2.4, and 3.6 m s^{-1} with negative values dashed. Fig. 9e is copied from Biggerstaff and Houze (1993).

3) POTENTIAL TEMPERATURE AND PRESSURE PERTURBATION

Direct measurements of temperature and pressure field at cloud-scale resolution are not available. Braun and Houze (1994) used the averaged dual-Doppler radar analysis to retrieve the pressure and potential temperature perturbations during the mature stage of the PRE-STORM case. Their retrievals are reproduced in Figs. 11c and 11f. The average potential temperature and pressure perturbations for the last 6 h of the simulations are plotted in Figs. 11a, 11b, 11d, and 11e for comparisons. Both spatial scales and contour lines are matched between the simulations and observations.

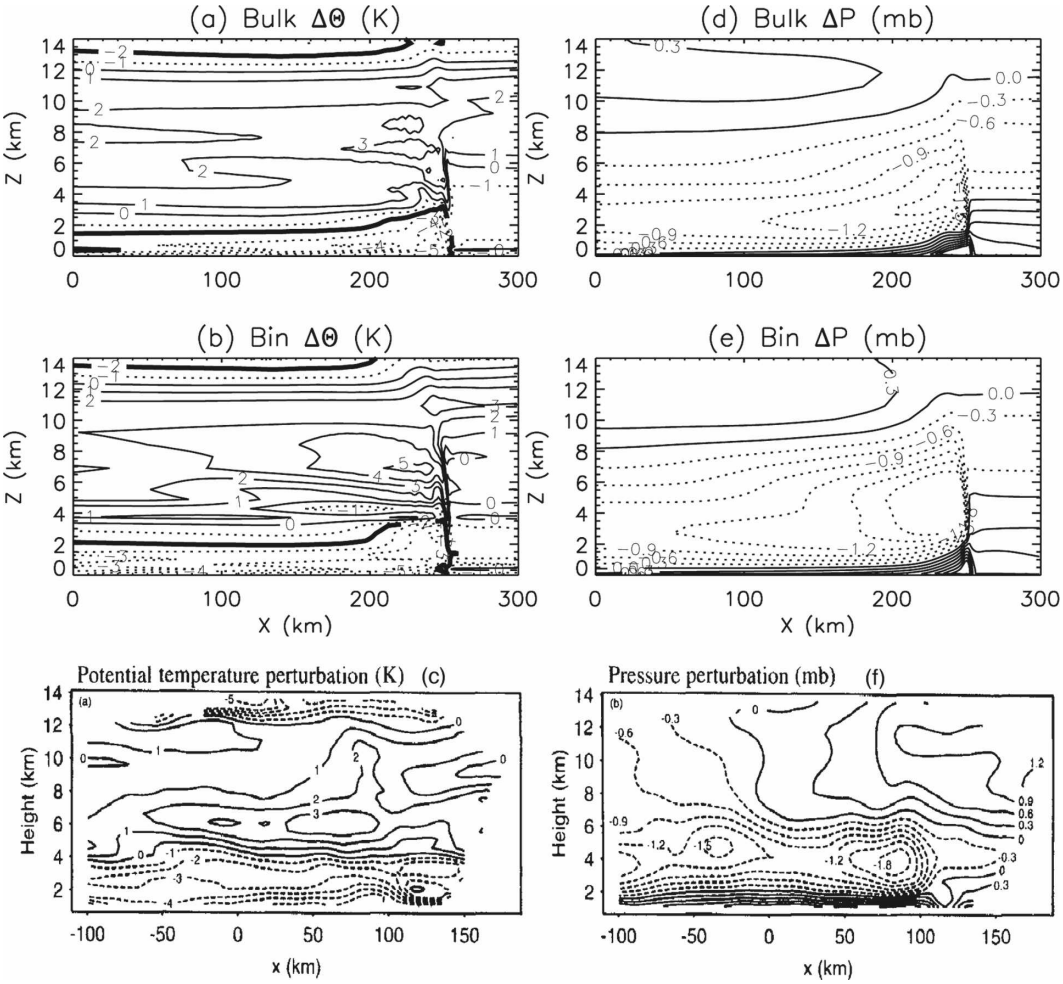

FIG. 11. Comparison of the (left) potential temperature and (right) pressure perturbations between the bulk and bin scheme simulations and the retrievals from Braun and Houze (1994): simulation plots are averaged over the last 6 h during the quasi-steady state. Potential temperature perturbations are for the (a) bulk simulation, (b) bin simulation, and (c) retrieval over the mature stage. Contour interval is 1 K with negative values dashed. The −2-K contour is thickened to indicate the near surface cool current. Pressure perturbations (mb) are plotted for the (d) bulk simulation, (e) bin simulation, and (f) retrieval at the same period as (c). The interval is 0.3 mb with negative values dashed. Both (c) and (f) are from Fig. 6 in Braun and Houze (1994). The spatial scales and the contour intervals for the simulations are matched to the retrievals.

The overall features in the potential temperature perturbation fields are very similar between the bulk (Fig. 11a) and bin simulation (Fig. 11b) and the retrieval (Fig. 11c). The three-layer structure shows cooling near the ground, mainly due to rain evaporation, a thick heating layer between 4 and 12 km produced by diabatic heating, and cooling again above 12 km, which is related to the ascent generated by the storm system at upper levels. For both simulations and the retrieval, the minimum potential temperature perturbation occurs near the gust front, with the lowest value of about −6 K. Both of the simulations of the cold current have a bulge near its head, which has also been simulated in previous model studies (e.g., Droegemeier and Wilhelmson 1987; Fovell and Dailey 1995). The absence of it in Fig. 11c may be due to the coarse resolution in the thermodynamic retrieval. The maximum heating at midlevels is about 3 K in the retrieval, compared with 3 K for the bulk simulation and 5 K for the bin simulation.

Average pressure perturbations (right column of Fig. 11) also agree with one another qualitatively. For example, the surface high-pressure center generated by the cold gust front is present in all three panels. Similarly, a surface pressure jump is also observed in Johnson and Hamilton (1988, their Fig. 13). Both the models and the retrieval show a wide mesolow at the midlevel, associated with the positively buoyant air

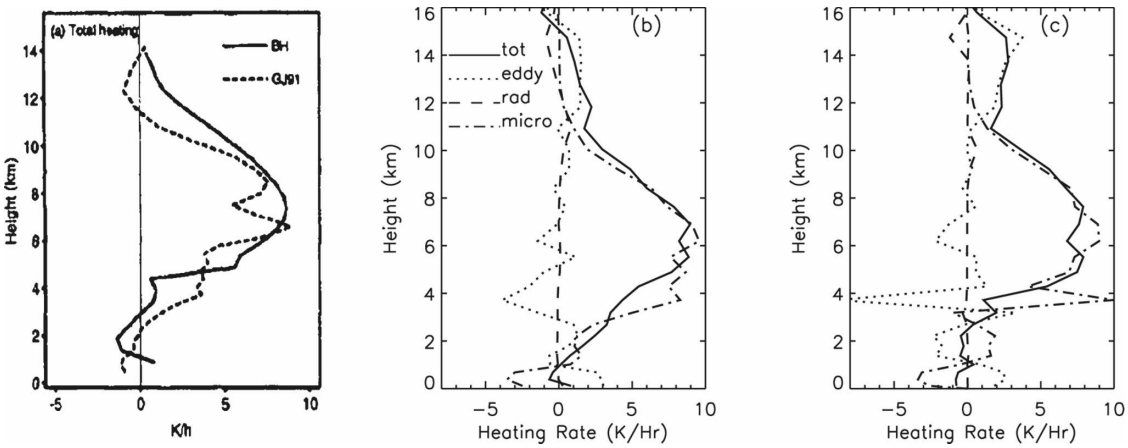

FIG. 12. Comparison of observed and simulated heating rate (K h^{-1}) profiles: (a) total heating rate averaged over the early (0030–0230 UTC) and mature (0300–0530 UTC) stage using Doppler radar observations (solid line; Braun and Houze 1996) and calculated by rawinsonde composites at 0300 UTC (dashed line; Gallus and Johnson 1991), copied from Fig. 18a in Braun and Houze (1996); total heating rate profiles (solid lines) averaged over the entire 12-h simulation period plotted for the (b) bulk and (c) bin schemes. Profiles of the three components of the total heating (eddy transport: dotted line; radiative heating: dashed line; microphysical heating: dashed–dotted line) are also shown for the simulations in (b) and (c).

(Houze 1993). The bin simulation has a deeper and wider mesolow, consistent with the simulated warmer potential temperature perturbation. At upper levels, both the bulk and bin scheme simulations show a weak thermodynamically driven high center above the thick, buoyant air at the top of the stratiform region. The retrieved horizontal pressure gradient at the upper levels in Fig. 11f is believed to be associated with a trough–ridge system in which the MCS is embedded. This synoptic-scale variation is not represented by the current CRM (Braun and Houze 1994; Zhang and Gao 1989). In addition, the double mesolow centers to the rear of the system shown in Fig. 11f are missing in both simulations.

c. Heat budget

Conventionally, the heat budget is represented by the apparent heat source (Q_1) in diagnostic studies (e.g., Yanai et al. 1973). In the PRE-STORM observation, the heat budget (Q_1) has been estimated using both a sounding network (Gallus and Johnson 1991) and a high-resolution Doppler radar retrieval (Braun and Houze 1996); Q_1 can also be explicitly calculated from CRMs (e.g., Tao et al. 2003b):

$$Q_1 = \overline{\pi}\left[-\frac{1}{\overline{\rho}}\frac{\partial \overline{\rho} w'\theta'}{\partial z} - \mathbf{V}' \cdot \nabla\theta' + D_\theta\right] + \left[\frac{L_v}{C_p}(c-e) + \frac{L_f}{C_p}(f-m) + \frac{L_s}{C_p}(d-s)\right] + Q_R, \quad (3)$$

where the first term on the rhs represents eddy heat flux convergence, the second term the microphysical heating, and the third term the radiative heating. In Eq. (3), $\overline{\pi}$ is the horizontal average of the nondimensional pressure, $\overline{\rho}$ the air density, $\mathbf{V}'$ and w' the perturbation horizontal wind vector and the vertical velocity, and D_θ the subgrid diffusion term. Parameters *c, e, f, m, d,* and *s* are rates of condensation, evaporation, freezing, melting, deposition, and sublimation. The CRM-simulated heat budget profiles using the two different microphysical schemes are plotted in Figs. 12b and 12c. The three terms in Eq. (3) are plotted separately, and the total heating is shown as solid lines. For comparison, the total apparent heating derived from Doppler radar observations (solid line) and a sounding network (dashed line) are reproduced in Fig. 12a. The sounding retrieval is the value, at 0300 UTC, during the mature stage of the PRE-STORM system. The Doppler radar retrieval is an average over 5 h, during the developing and the mature stage of the same storm. The simulations in Figs. 12b and 12c are averaged over the whole 12-h simulation period. To match the observations, only heating profiles over the rain area are averaged in the simulations.

By far, the dominant heating term in Figs. 12b and 12c is the microphysical heating. Because the PRE-STORM case occurred during nighttime, the radiative term is negligible except for the longwave cooling at cloud tops. Eddy fluxes are only important near the cloud top and cloud base. Comparing the total simulated Q_1 (the solid lines in Figs. 12b and 12c) with

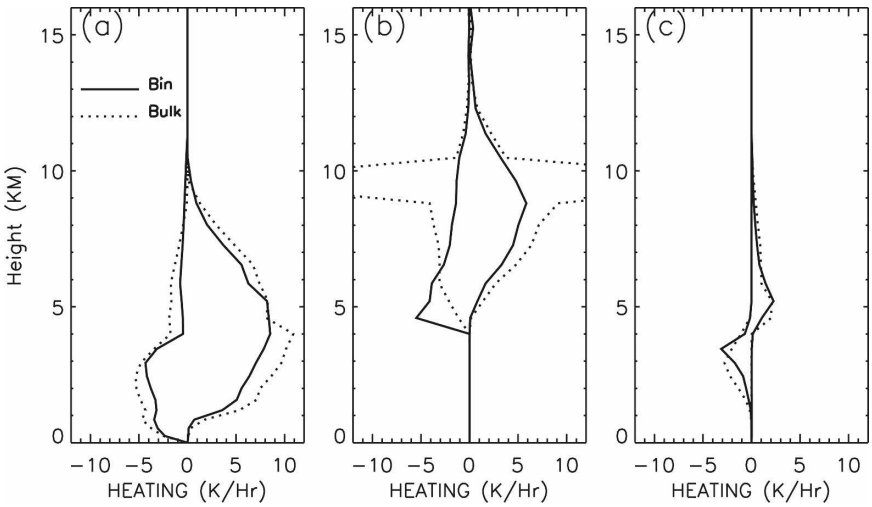

FIG. 13. Components of the microphysical heating profiles simulated by the bulk (dashed lines) and bin (solid lines) scheme: (a) condensation and evaporation, (b) deposition and sublimation, and (c) melting and freezing.

observations (Fig. 12a), there is a general agreement in the total profiles. Nonetheless, there are some discrepancies between the observations and simulations. For example, both of the observed heating profiles have their maxima located between 7 and 9 km and they decrease monotonically above and below that level. The simulated maximum heating level is lower than in the observations, at around 6 km in the bulk simulation and 7 km in the bin simulation. The lower position of the heating maxima is consistent with the lower simulated rear inflow height and the lower maximum w center in both simulations (cf. Figs. 4 and 10), which can be partly attributed to the 2D modeling framework used in this study.

Profiles of the six individual microphysical heating terms—condensation, evaporation, deposition, sublimation, melting, and freezing—are plotted in Fig. 13 to show the differences between the two microphysical schemes in more detail. The summation of these terms is the microphysical heating term represented by the dash–dotted line in Figs. 12b and 12c. In Fig. 13a, condensation is smaller at lower levels in the bin simulation but larger at upper levels because the bin simulation has a more upright and deeper leading convective core than the bulk simulation. The bulk simulation has more evaporation at all levels. For both simulations, rain evaporation (below 4 km) is much larger compared with cloud evaporation (above 4 km). There is stronger sublimation in the bin simulation at around 5 km (Fig. 13b) because of the larger size anvil simulated by the bin scheme. The large spikes in both deposition and sublimation at around 10 km in the bulk simulation are produced artificially by limitations in the saturation adjustment scheme in the bulk scheme. These two spikes largely cancel each other and have little effect on the total energy budget.

Rain efficiency is another important quantity in the large-scale impact of a squall system and in cumulus parameterization schemes. Here the rain efficiency is defined as the ratio of the total surface rainfall and the summation of the total condensation and deposition (e.g., Tao et al. 2004). In tilted systems (such as in the bulk PRESTORM case simulation), the rain shaft is more detached from the strongest updraft core, causing more rain evaporation in such systems and reducing the rain efficiency (e.g., Ferrier et al. 1996) compared with more upright systems (such as in the bin simulation). Rain efficiencies are 31.8% for the bulk simulation and 37.3% for the bin simulation, consistent with the previous studies.

4. Summary and future work

A well-documented midlatitude summertime MCS is simulated using the GCE model with two microphysical schemes: a simple, well-established bulk scheme and a newly incorporated spectral bin scheme that explicitly resolves the size distributions of cloud/rain, snow aggregates, graupel, hail, and three types of ice crystals (column, plate, and dendrite). Identical initial and environmental conditions ensure that the sensitivities of the simulations are due only to the different representations of cloud microphysics and subsequent microphysics–dynamics interactions. The model is run for a total of 12 h, which includes about 6 h in its quasi-steady state. The emphasis of this paper is on describing dif-

ferences between the bulk and bin scheme simulations, especially during the quasi-steady state. Also, published observations and observation-based retrievals of the same PRE-STORM case are included as much as possible so as to validate the simulations.

Significant differences exist during the quasi-steady state of simulations using the bulk and bin schemes, especially in high-resolution temporal variations. The convective cell regeneration and propagation take two distinct temporal and spatial variation modes. In terms of temporal variations, the bin simulation shows a weak evolution mode for which the leading cell undergoes internal oscillations without explicit new cell regenerations. On the other hand, the bulk simulation has a strong evolution mode for which the leading cell goes through a distinct life cycle and more discrete propagation. In terms of spatial variations, the bin simulation produces a unicell storm in which one deep convective core with relatively upright orientation dominates the convective region. The quasi-steady state simulated by the bulk scheme, however, consists of a much shallower leading convection tilting rearward, trailed by four or five convective cells (termed a multicell storm), some extend well into the stratiform region. These cells are rearward propagating, previous leading cells that become progressively weaker as they move away from the storm's leading edge. The stratiform region simulated by the bin scheme is much wider and contributes to about 20% of the total surface rainfall, compared with a narrow stratiform region that contributes to only 7% of the total rainfall in the bulk simulation. The bin scheme simulated stratiform region is horizontally homogeneous, with mesoscale weak uplift of less than 1 m s^{-1} above the melting level and weak downward motion below it. The bulk simulation, however, shows weak convective cells embedded in its stratiform region with the presence of liquid cloud water. The available PRE-STORM observations did not definitely support the categorization of unicell versus multicell storm or weak versus strong evolution mode, and whether there are embedded cells in the stratiform region. However, the bin simulation agrees better with both instantaneous and time-averaged radar observations. All of these contrasting features (multicell versus unicell, weak versus strong evolution) have been previously observed in different systems and various environmental conditions. The fact that they are simulated in the same case by varying only the microphysical scheme indicates the significant role microphysics can play in shaping the storm structure and dynamics.

Despite our emphasis on differences in the two sets of simulations, the evolution of the simulated MCSs and many of their structures remain similar. For example, both storms have well-defined convective and stratiform regions. The flow patterns, especially after being time averaged, are quite similar and compare well with the observations. The magnitude and structure of both the averaged potential temperature and pressure perturbations agree with each other, also with the retrievals. The large-scale influences generated by the simulated storms, for example, the apparent heat source, moisture sink, and vertical mass fluxes profiles, are all similar for the two simulations, as well as the available retrievals.

Both bulk and bin microphysical schemes—as well as a suite of multimoment bulk scheme in between—involve various assumptions and have their own strengths and shortcomings. Detailed comparisons of these schemes are necessary to gain knowledge and confidence in using them for different applications. For this particular case, it is found that for the estimation of mean heating profiles, total energy, or momentum contributions of a continental MCS to its environmental flow, both bulk and bin schemes work well. However, for high-resolution storm forecasting and flood warning, or accurate retrieval algorithms of remote sensing, proper representations of various microphysical processes become crucial.

In the second part of this paper, further diagnostic analyses and sensitivity tests are performed to study interactions between cloud microphysics and dynamics and the mechanisms that produce sensitivities described in this paper. It is hoped that these comparisons and analyses will eventually lead to a better understanding of the microphysics–dynamics interactions in an MCS and to improvements in both the bulk and bin microphysical schemes. However, this goal will not be achieved without high-resolution observations together with detailed, in situ microphysical observations.

Acknowledgments. The authors wish to thank Dr. Chung-Lin Shie for his help in calculating the budgets and Stephen Lang for proofreading. Constructive suggestions from Professor Robert Fovell and four anonymous reviewers have greatly improved this paper. This research is mainly supported by the NASA headquarters and the NASA TRMM Mission. The authors are grateful to Dr. R. Kakar at NASA headquarters for his support of this research. Acknowledgement is also made to NASA GSFC for computer time used in this research.

REFERENCES

Biggerstaff, M. I., and R. A. Houze Jr., 1993: Kinematics and microphysics of the transition zone of the 10–11 June 1985 squall line. *J. Atmos. Sci.,* **50,** 3091–3110.

Bott, A., 1998: A flux method for the numerical solution of the stochastic collection equation. *J. Atmos. Sci.,* **55,** 2284–2293.

Braun, S. A., and R. A. Houze Jr., 1994: The transition zone and secondary maximum of radar reflectivity behind a midlatitude squall line: Results retrieved from Doppler radar data. *J. Atmos. Sci.,* **51,** 2733–2755.

——, and ——, 1996: The heat budget of a midlatitude squall line and implications for potential vorticity production. *J. Atmos. Sci.,* **53,** 1217–1240.

Carrió, G. G., and M. Nicolini, 2002: An alternative procedure to evaluate number concentration rates in two-moment bulk microphysical schemes. *Atmos. Res.,* **65,** 93–108.

Clark, T. L., 1973: Numerical modeling of the dynamics and microphysics of warm cumulus convection. *J. Atmos. Sci.,* **30,** 857–878.

Cotton, W. R., G. J. Tripoli, R. M. Rauber, and E. A. Mulvihill, 1986: Numerical simulation of the effects of varying ice crystal nucleation rates and aggregation processes on orographic snowfall. *J. Climate Appl. Meteor.,* **25,** 1658–1680.

Droegemeier, K. K., and R. B. Wilhelmson, 1987: Numerical simulation of thunderstorm outflow dynamics. Part I: Outflow sensitivity experiments and turbulence dynamics. *J. Atmos. Sci.,* **44,** 1180–1210.

Ferrier, B. S., 1994: A double-moment multiple-phase four-class bulk ice scheme. Part I: Description. *J. Atmos. Sci.,* **51,** 249–280.

——, J. Simpson, and W.-K. Tao, 1996: Factors responsible for precipitation efficiencies in midlatitude and tropical squall simulations. *Mon. Wea. Rev.,* **124,** 2100–2125.

Foote, G. B., and H. W. Frank, 1983: Case study of a hailstorm in Colorado. Part III: Airflow from triple-Doppler measurements. *J. Atmos. Sci.,* **40,** 686–707.

Fovell, R. G., and Y. Ogura, 1989: Effect of vertical wind shear on numerically simulated multicell storm structure. *J. Atmos. Sci.,* **46,** 3144–3175.

——, and P. S. Dailey, 1995: The temporal behavior of numerically simulated multicell-type storms. Part I: Modes of behavior. *J. Atmos. Sci.,* **52,** 2073–2095.

——, and P.-H. Tan, 1998: The temporal behavior of numerically simulated multicell-type storms. Part II: The convective cell life cycle and cell regeneration. *Mon. Wea. Rev.,* **126,** 551–577.

——, G. L. Mullendore, and S.-H. Kim, 2006: Discrete propagation in numerically simulated nocturnal squall lines. *Mon. Wea. Rev.,* **134,** 3735–3752.

Fridlind, A. M., and Coauthors, 2004: Evidence for the predominance of mid-tropospheric aerosols as subtropical anvil cloud nuclei. *Science,* **304,** 718–722.

Gallus, W. A., and R. H. Johnson, 1991: Heat and moisture budgets of an intense midlatitude squall line. *J. Atmos. Sci.,* **48,** 122–146.

Hall, W. D., 1980: A detailed microphysical model within a two-dimensional dynamical framework: Model description and preliminary results. *J. Atmos. Sci.,* **37,** 2486–2507.

Hallett, J., and S. C. Mossop, 1974: Production of secondary ice particles during the riming process. *Nature,* **249,** 26–28.

Houze, R. A., Jr., 1993: *Cloud Dynamics.* Academic Press, 573 pp.

Johnson, R. H., and P. J. Hamilton, 1988: The relationship of surface pressure features to the precipitation and airflow structure of an intense midlatitude squall line. *Mon. Wea. Rev.,* **116,** 1444–1472.

Kessler, E., III, 1969: *On the Distribution and Continuity of Water Substance in Atmospheric Circulation. Meteor. Monogr.,* No. 32, Amer. Meteor. Soc., 84 pp.

Khain, A. P., and I. Sednev, 1996: Simulation of precipitation formation in the eastern Mediterranean coastal zone using a spectral microphysics cloud ensemble model. *Atmos. Res.,* **43,** 77–110.

——, A. Pokrovsky, and I. Sednev, 1999: Some effects of cloud–aerosol interaction on cloud microphysics structure and precipitation formation: Numerical experiments with a spectral microphysics cloud ensemble model. *Atmos. Res.,* **52,** 195–220.

——, M. Ovtchinnikov, M. Pinsky, A. Pokrovsky, and H. Krugliak, 2000: Notes on the state-of-the-art numerical modeling of cloud microphysics. *Atmos. Res.,* **55,** 159–224.

——, A. Pokrovsky, M. Pinsky, A. Seifert, and V. Phillips, 2004: Simulation of effects of atmospheric aerosols on deep turbulent convective clouds using a spectral microphysics mixed-phase cumulus cloud model. Part I: Model description and possible applications. *J. Atmos. Sci.,* **61,** 2963–2982.

——, D. Rosenfeld, and A. Pokrovsky, 2005: Aerosol impact on the dynamics and microphysics of deep convective clouds. *Quart. J. Roy. Meteor. Soc.,* **131,** 2639–2663.

Klemp, J. B., and R. B. Wilhelmson, 1978: The simulation of three-dimensional convective storm dynamics. *J. Atmos. Sci.,* **35,** 1070–1096.

Kogan, Y. L., 1991: The simulation of a convective cloud in a 3-D model with explicit microphysics. Part I: Model description and sensitivity experiments. *J. Atmos. Sci.,* **48,** 1160–1189.

Li, X., W.-K. Tao, A. P. Khain, J. Simpson, and D. E. Johnson, 2009: Sensitivity of a cloud-resolving model to bulk and explicit bin microphysical schemes. Part II: Cloud microphysics and storm dynamics interactions. *J. Atmos. Sci.,* **66,** 22–40.

Lin, Y.-L., and L. E. Joyce, 2001: A further study of the mechanisms of cell regeneration, propagation, and development within two-dimensional multicell storms. *J. Atmos. Sci.,* **58,** 2957–2988.

——, R. D. Farley, and H. D. Orville, 1983: Bulk parameterization of the snow field in a cloud model. *J. Climate Appl. Meteor.,* **22,** 1065–1092.

Lynn, B. H., A. P. Khain, J. Dudhia, D. Rosenfeld, A. Pokrovsky, and A. Seifert, 2005: Spectral (bin) microphysics coupled with a mesoscale model (MM5). Part II: Simulation of a CaPE rain event with a squall line. *Mon. Wea. Rev.,* **133,** 59–71.

Meyers, M. P., P. J. DeMott, and W. R. Cotton, 1992: New primary ice-nucleation parameterizations in an explicit cloud model. *J. Appl. Meteor,* **31,** 708–721.

——, R. L. Walko, J. Y. Harrington, and W. R. Cotton, 1997: New RAMS cloud microphysics parameterization. Part II: The two-moment scheme. *Atmos. Res.,* **45,** 3–39.

Morrison, H., and W. W. Grabowski, 2007: Comparison of bulk and bin warm-rain microphysics models using a kinematic framework. *J. Atmos. Sci.,* **64,** 2839–2861.

Murakami, M., 1990: Numerical modeling of dynamical and microphysical evolution of an isolated convective cloud—The 19 July 1981 CCOPE cloud. *J. Meteor. Soc. Japan,* **68,** 107–128.

Ovtchinnikov, M., and Y. L. Kogan, 2000: An investigation of ice production mechanisms in small cumuliform clouds using a 3D model with explicit microphysics. Part I: Model description. *J. Atmos. Sci.,* **57,** 2989–3003.

——, ——, and A. M. Blyth, 2000: An investigation of ice production mechanisms in small cumuliform clouds using a 3D

model with explicit microphysics. Part II: Case study of New Mexico cumulus clouds. *J. Atmos. Sci.,* **57,** 3004–3020.

Pandya, R. E., and D. R. Durran, 1996: The influence of convectively generated thermal forcing on the mesoscale circulation around squall lines. *J. Atmos. Sci.,* **53,** 2924–2951.

Parker, M. D., and R. H. Johnson, 2004: Simulated convective lines with leading precipitation. Part I: Governing dynamics. *J. Atmos. Sci.,* **61,** 1637–1655.

Phillips, V. T. J., A. Pokrovsky, and A. Khain, 2007: The influence of time-dependent melting on the dynamics and precipitation production in maritime and continental storm clouds. *J. Atmos. Sci.,* **64,** 338–359.

Pruppacher, H. R., and J. D. Klett, 1997: *Microphysics of Clouds and Precipitation.* 2nd ed. Kluwer Academic, 954 pp.

Reisin, T., Z. Levin, and S. Tzivion, 1996: Rain production in convective clouds as simulated in an axisymmetric model with detailed microphysics. Part I: Description of the model. *J. Atmos. Sci.,* **53,** 497–519.

Rutledge, S. A., and D. R. MacGorman, 1988: Cloud-to ground lightening activity in the 10–11 June 1985 mesoscale convective system observed during the Oklahoma–Kansas PRE-STORM project. *Mon. Wea. Rev.,* **116,** 1393–1408.

——, and W. A. Petersen, 1994: Vertical radar reflectivity structure and cloud-to ground lightning in the stratiform region of MCSs: Further evidence for in situ charging in the stratiform region. *Mon. Wea. Rev.,* **122,** 1760–1776.

——, R. A. Houze Jr., and M. I. Biggerstaff, 1988: The Oklahoma–Kansas mesoscale convective system of 10–11 June 1985: Precipitation structure and single-Doppler radar analysis. *Mon. Wea. Rev.,* **116,** 1409–1430.

Seifert, A., and K. D. Beheng, 2006: A two-moment cloud microphysics parameterization for mixed-phase clouds. Part 1: Model description. *Meteor. Atmos. Phys.,* **92,** 45–66.

Shiino, J., 1983: Evolution of raindrops in an axisymmetric cumulus model. Part I: Comparison of the parameterized with nonparameterized microphysics. *J. Meteor. Soc. Japan,* **61,** 629–655.

Smolarkiewicz, P. K., and W. W. Grabowski, 1990: The multidimensional positive definite advection transport algorithm: Nonoscillatory option. *J. Comput. Phys.,* **86,** 355–375.

Smull, B. F., and R. A. Houze Jr., 1987a: Dual-Doppler radar analysis of a midlatitude squall line with a trailing region of stratiform rain. *J. Atmos. Sci.,* **44,** 2128–2149.

——, and ——, 1987b: Rear inflow in squall lines with trailing stratiform precipitation. *Mon. Wea. Rev.,* **115,** 2869–2889.

Soong, S., 1974: Numerical simulation of warm rain development in an axisymmetric cloud model. *J. Atmos. Sci.,* **31,** 1262–1285.

Szeto, K. K., and H.-R. Cho, 1994: A numerical investigation of squall lines. Part I: The control experiment. *J. Atmos. Sci.,* **51,** 414–424.

Takahashi, T., 1975: Tropical showers in an axisymmetric cloud model. *J. Atmos. Sci.,* **32,** 1318–1330.

Tao, W.-K., and J. Simpson, 1993: Goddard Cumulus Ensemble Model. Part I: Model description. *Terr. Atmos. Oceanic Sci.,* **4,** 35–72.

——, ——, C.-H. Sui, B. Ferrier, S. Lang, J. Scala, M.-D. Chou, and K. Pickering, 1993: Heating, moisture, and water budgets of tropical and midlatitude squall lines. Comparisons and sensitivity to longwave radiation. *J. Atmos. Sci.,* **50,** 673–690.

——, S. Lang, J. Simpson, C.-H. Sui, B. Ferrier, and M.-D. Chou, 1996: Mechanisms of cloud–radiation interaction in the tropics and midlatitudes. *J. Atmos. Sci.,* **53,** 2624–2651.

——, and Coauthors, 2003a: Microphysics, radiation, and surface processes in the Goddard Cumulus Ensemble (GCE) model. *Meteor. Atmos. Phys.,* **82,** 97–137.

——, C.-L. Shie, J. Simpson, S. Braun, R. H. Johnson, and P. E. Ciesielski, 2003b: Convective systems over the South China Sea: Cloud-resolving model simulations. *J. Atmos. Sci.,* **60,** 2929–2955.

——, X. Li, A. Khain, T. Matsui, S. Lang, and J. Simpson, 2007: Role of atmospheric aerosol concentration on deep convective precipitation: Cloud-resolving model simulations. *J. Geophys. Res.,* **112,** D24S18, doi:10.1029/2007JD008728.

Torrence, C., and G. P. Compo, 1998: A practical guide to wavelet analysis. *Bull. Amer. Meteor. Soc.,* **79,** 61–78.

Twomey, S., and T. A. Wojciechowski, 1969: Observations of the geographical variation of cloud nuclei. *J. Atmos. Sci.,* **26,** 684–688.

Vali, G., 1975: Remarks on the mechanism of atmospheric ice nucleation. *Proc. Eighth Int. Conf. on Nucleation,* Leningrad, Russia, ICCP, 265–269.

Wang, C., and J. S. Chang, 1993: A three-dimensional numerical model of cloud dynamics, microphysics, and chemistry. 1. Concepts and formulation. *J. Geophys. Res.,* **98** (D8), 14 827–14 844.

Weisman, M. L., J. B. Klemp, and R. Rotunno, 1988: Structure and evolution of numerically simulated squall lines. *J. Atmos. Sci.,* **45,** 1990–2013.

Yanai, M., S. Esbensen, and J. Chu, 1973: Determination of bulk properties of tropical cloud clusters from large-scale heat and moisture budgets. *J. Atmos. Sci.,* **30,** 611–627.

Yang, M.-J., and R. A. Houze Jr., 1995: Multicell squall-line structure as a manifestation of vertically trapped gravity waves. *Mon. Wea. Rev.,* **123,** 641–661.

Yin, Y., Z. Levin, T. G. Reisin, and S. Tzivion, 2000a: Seeding convective clouds with hygroscopic flares: Numerical simulations using a cloud model with detailed microphysics. *J. Appl. Meteor.,* **39,** 1460–1472.

——, ——, ——, and ——, 2000b: The effects of giant cloud condensation nuclei on the development of precipitation in convective clouds—A numerical study. *Atmos. Res.,* **53,** 91–116.

Zhang, D.-L., and K. Gao, 1989: Numerical simulation of an intense squall line during 10–11 June 1985 PRE-STORM. Part II: Rear inflow, surface pressure perturbations, and stratiform precipitation. *Mon. Wea. Rev.,* **117,** 2067–2094.